A MOMENTUM SPECTRUM FOR HIGH ENERGY MESOTRONS

Thesis by

George Michael Safonov

In Partial Fulfillment of the Requirements

For the Degree of

Doctor of Philosophy

California Institute of Technology

Pasadena, California

1949

The author wishes to express his deepest appreciation for the guidance and encouragement given him by Professor Carl D. Anderson.

During the recent war and for the last several years, the author has had the privilege of working under the supervision of both Professors Anderson and W. R. Smythe. This association has served to inspire him to continue his education and has sharpened his sincere interest in physics.

It is with pleasure that the writer acknowledges the early work in creating the instrument used in these investigations. Contributors to this task have been Dr. Bernard Hamermesh and Mr. Donald Glaser.

ABSTRACT

By means of a two cloud chamber technique, a differential momentum spectrum was obtained for mesotrons with momentum up to ~ 40 billion electron volts. The existence of individual particles with energies of 16 billion electron volts is found by direct measurements. We find an apparent 20% positive excess of mesotrons moving in a nearly vertical direction.

A technical description of the instrument is given along with the theory of its operation.

TABLE OF CONTENTS

INTRODUCTION

Since the work of Anderson and Neddermeyer (1) in 1934, there have been continued efforts to extend our knowledge of cosmic ray momentum spectra to higher and higher energies. Le Prince-Ringuet (2), Blackett (3), Jones (4), Hughes (5), and Wilson (6) have made major contributions toward the achievement of this end.

The limit of momentum resolution achieved up to the present time is about 20 BeV*, that is, the instruments used thus far have been unable to distinguish between a particle with 20 BeV momentum and one with infinite momentum. The accurate production and measurement of a truly representative particle trajectory in a cloud chamber has always been a limiting factor. This and the small curvatures caused by the magnetic fields available have restricted the range of investigation.

The techniques of previous workers have a point in common. All have used a single cloud chamber immersed in a magnetic field for the study of singly occurring particles.

The following text describes a technique employing two cloud chambers. These are placed above and below a magnetic field. Observation of the deflection of a particle passing through both chambers allows the computation of its momentum. The fact that the chambers are out of the field provides certain advantages. It is possible to concentrate a strong field in a small but efficiently used gap without an excessively large magnet. Also,

---

*The momentum, P , of a particle multiplied by c, the velocity of light yields a quantity, Pc , which has the dimensions of energy. This quantity is numerically proportional to the momentum and is therefore a measure of the momentum. In this text we call out momenta in terms of Pc which we give in units of BeV, billions of electron volts. From this convention, one would obtain P in units of c.g.s. by multiplying by $.533 \times 10^{-13}$.

the magnetic field of such an arrangement cuts out a large amount of the soft component. It is a simple matter to enclose each chamber in a thermally isolated box, thus shielding it from the distortion-producing heat of the magnet coils. Each chamber may be photographed through a lens utilizing a small angle of view, thus making possible an accurate recording of the tracks. Photography in a magnetic field is usually accomplished with wide angle lenses set close to the chamber. This is to avoid a large gap with a consequent loss in field strength. A minor advantage of the two-chamber technique is the simplicity of computation for the aperture of the instrument to particles of various momenta (see Appendix A).

An apparent disadvantage is the possibility of deflecting or scattering a particle in the material separating the two chambers. This possibility is shown to be remote in the section on "Discussion of Errors."

It has been possible to double the past range of investigation with such a technique; hence, particles with 40 BeV momentum may be distinguished from those with infinite momentum. With a higher resolution available, we have made a preliminary investigation of the high energy component of sea level radiation.

THEORY OF EXPERIMENTAL PROCEDURE

The distribution of momenta among cosmic ray particles is usually described by means of a function $I(P)$. $I(P)$ is defined by the equation

$$(1) \quad dN = I(P) \cdot t \cdot dA \cdot d\Omega \cdot dP$$

In equation (1), dN is the number of particles that pierce the area dA in time t. The momentum of each member of the group, dN, lies in the interval dP about P. The various directions of entry are included in the solid angle $d\Omega$ about the normal to dA.

To experimentally determine $I(P)$, it is necessary to account for the number, N, and momenta, P, of the particles that pass through an instrument. These data and a proper interpretation of the "aperture" of the instrument permit the computation of $I(P)$. N and P are determined for singly occurring charged particles by means of the instrument sketched in Figure 1.

G_1, G_2 are identical Geiger tubes held with their cylindrical axes horizontal and parallel. G_1 is a distance D directly above G_2. Each tube has a useful length W and a diameter T. It is noted from Figure 1 that W and T are small compared to D.

The tubes, working in coincidence, can enumerate the ionizing particles that pass through the system. If it were possible to determine P for each of these particles, $I(P)$ could be found from equation (1) as

$$(2) \quad I(P) \cong \frac{1}{t}\left(\frac{D}{WT}\right)^2 \frac{dN}{dP}$$

In a region midway between G_1, G_2 is a magnetic field. The direction of the field is normal to the plane defined by the axes of G_1, G_2. The magnitude of the field is essentially uniform in the region of length L

(see Figure 1). Elsewhere the field is weak and negligible.

C_1, C_2 are cloud chambers situated in the field free spaces just below G_1 and above G_2. C_1, C_2 are viewed by cameras with their lens axes parallel to the magnetic field.

The trajectory of a particle detected by G_1, G_2 is indicated in the figure. In C_1 it is rectilinear. It is continually deflected as it passes through the region of the magnetic field. Finally it passes through C_2 along a linear path.

The operation of the instrument is initiated by a coincidence signal from G_1, G_2. This causes the expansion of C_1, C_2 and the eventual photography of the tracks produced. The net deflection of the trajectory is observed in the photographs. This observation together with a knowledge of the field permit a computation for the momentum of the particle.

Since both N and P may be determined by the device, it is possible to determine $I(P)$. However the magnetic field between G_1, G_2 gives the instrument certain selective properties. That is, it may now partially or completely exclude particles that would pass through it in the absence of the field. For this reason, equation (2) must be modified to

$$(3) \quad I(P) = \frac{\gamma}{t}\left(\frac{D}{WT}\right)^2 \frac{dN}{dP}$$

Above γ is a factor depending on the momentum, P, and the charge e of the particles considered. γ is also a function of the geometry of the instrument used. γ is evidently a correction or weighting factor that compensates for the selectivity introduced by the magnetic field. The number of particles, dN, with momenta between P and $P + dP$ that pass through the instrument is proportional to $\frac{1}{\gamma}\left(\frac{WT}{D}\right)^2$. This quantity may be appropriately termed the aperture of the instrument. The aperture for no magnetic field is $\left(\frac{WT}{D}\right)^2$; thus $\frac{1}{\gamma}$ would be the relative aperture.

A general equation for γ as a function of the momentum and of various geometrical parameters is derived in Appendix A. The relative aperture of the instrument under the conditions used is shown in Figure 2. The magnetic cut-off value of .3 BeV has been quite well confirmed; the lowest momentum measured is .351 BeV. The relative aperture for weaker particles is seen to be less than $\frac{1}{50}$. We note that beyond 1.3 BeV the relative aperture is sensibly constant. Thus the correction to be applied is small for momenta greater than 1.3 BeV. Between .3 and 1.3 BeV the relative aperture varies widely. Unfortunately this is in the region where it is most difficult to determine $\frac{dN}{dP}$ accurately and one must apply the correction with caution. This does not hinder the progress of the present work which is aimed primarily at the investigation of high momenta. Putting $\gamma = 1$ in equation (3), does not appreciably alter the determination of $I(P)$.

If φ be the net angular deflection of a particle with charge e caused by the field, then its momentum P is approximately

$$(4) \qquad P = \frac{eK}{\varphi}$$

This equation is derived in Appendix B. K is the deflection constant of the magnetic field; it has the dimensions of gauss centimeters when e is in e.m.u. and P is in c.g.s. A simple and unique method of determining this constant is given in Appendix B. Under the conditions of the experiment, P may be found in BeV from

$$(5) \qquad P = \frac{.126}{\varphi}$$

where φ is expressed in radians.

φ is measured from the photographs of the two chambers. The essence of this measurement involves the reprojection of a picture of the track and a fine vertical reference wire. The angle between the track and wire is determined for each chamber; the differences between these two angles is φ.

A rigorous equation treating the determination of φ stereoscopically is given in Appendix C.

Figure 3 shows photographs of a typical track passing through the apparatus.

Having determined P for several tracks, we enumerated the particles according to increasing momenta. A plot of the number assigned to each particle versus its momentum is called an integral spectrum. The slope of the integral spectrum $\frac{dN}{dP}$ gives the desired differential spectrum.

It might be noticed from Figure 11 that at 150 amperes the nominal field strength is 12.5×10^3 gauss. Thus at four times the power it is only possible to obtain a field increase of about 25%. At this high current, the heat from the magnet coils may cause objectional distortions in the cloud chambers. The resolution gained by higher fields is more than canceled by the inability to produce straight tracks in the chambers.

While in operation the magnet coils were protected by a circuit breaker which could be activated by various safety devices. These included two water-flow switches, a water temperature thermostat, and a circuit which detected a radical imbalance in voltage across the four coils. A series of selenium rectifiers absorbed the large magnetic field energy when the circuit was disrupted.

Parts of the magnet are visible in Figures 15 and 16.

THE CLOUD CHAMBERS

The cloud chambers C_1, C_2 (see Figure 1) are about 30 cm in diameter and 10 cm deep. A typical chamber is shown in Figure 18. The expansion is due to the movement of a piston which is connected to the chamber proper by means of a 1/16 inch rubber diaphragm. The chamber mixture is argon with saturated vapor of absolute alcohol. The total pressure of the mixture is about 8 pounds per square inch when the chamber is in the unexpanded position. The piston is held "cocked" in this position by means of a solenoid-operated mechanical latch. The discharge of some 100 microfarads at an initial voltage of $\sim$ 500 volts activates the solenoid and causes the expansion. A sweep field voltage of $\sim$ 100 volts is continually applied between the body of the chamber and an aquadag ring painted on the cylindrical glass piece (see Figure 18). This clearing potential is disrupted only upon expansion.

The chambers are recompressed and cocked by means of air pressure (greater than the internal pressure) being applied behind the pistons. This pressure is discontinued when the pistons are in the compressed position and the mechanical holding latch is again engaged.

Expansion ratios of about 1/10 are used.

Illumination during photography is due to a rapid condenser discharge through gas-filled tubes. Each gas tube is about 14 inches long and 1/2 inch in diameter. The light is concentrated into a beam by a bank of three 4 inch diameter condensing lenses. The beam enters the chamber at 90 degrees to its axis. Black velvet mounted on a grid inside the chamber forms a background for sharp contrast during the photography.

Great precautions were taken to insulate the chambers from possible heat emanating from the magnet coils. To minimize this possibility and to protect the chambers from local drafts a box enclosed each chamber and its two cameras. The box was built of 3/8 inch plywood with 1/2 to 1 inch of glass wool insulation as an inner lining.

THE CAMERAS

Two 35 mm recording cameras are used to photograph each cloud chamber. Thus, a total of four cameras view the two chambers. This battery of cameras is shown in Figure 17. Each camera holds 100 feet of film, 3/4 inch being required for each exposure. The film is moved by means of an air piston after each exposure; thereby being ready for the next. The lenses used are 4 inch f/4.5 Ektar made by Kodak. In operation, the lenses were left open continuously at f/4.5. The shutter action during photography is due to the rapid firing of the gas-filled flash lamps. The half angle of view subtended by the chamber is about 6 degrees. At this small view angle, lens distortions are entirely negligible.

The front nodal point of each camera is about 140 cm distant from the face of its cloud chamber. The axes of the two cameras viewing a single chamber are at the horizontal level of the chamber and spaced 25 cm apart. One camera views the chamber directly down the chamber axis. The second camera obtains an oblique view of the chamber at a stereoscopic angle of 10 degrees. The pair of pictures thus taken give data leading to the computation of the desired trajectory angle. The measurements from which this angle may be computed are discussed in Appendix C.

Beside photographing the chambers, each camera recorded a number on a mechanical counter. This number enumerates the pictures and allows the correct pairing of pictures.

The film used is the fast Eastman Linograph Orthochromatic. It is developed for about 6 minutes in Eastman D-19 developer at normal room temperatures.

THE CYCLING PROCESS

The operation of the instrument is completely automatic. Once the chambers are properly set and in temperature equilibrium, the following cycle is initiated by a coincidence signal from the Geiger tubes:

a. The solenoids trip the mechanical latches holding the chambers cocked; thus the internal pressure displaces the chamber piston and an expansion results;

b. The displacement of the mechanical holding latch opens a switch which cuts off the sweep voltage;

c. The switch mentioned in b. starts a two-minute timer. Two minutes is the "dead time" of the chamber. During this interval, no coincidence detected by the Geiger tubes may set off a cycle.

d. After the $\sim 1/40$ of a second taken for the mechanical latch to experience its full displacement, a second switch is engaged which causes the flash lamps to illuminate the scene of the track; thus the photography is complete.

e. In the following 15 seconds, the chambers are reset and the clearing potential is again applied.

f. At this same time (as event e.) the films in the cameras are rolled into a position awaiting the next exposure. Also, the mechanical counter indicating the picture number is changed.

g. Finally, approximately 2 minutes after the expansions, the dead time mechanism again permits coincident counts to initiate a cycle.

THE PROJECTION AND MEASUREMENT

Figure 19 shows two projectors which throw a full size image of each chamber onto a table. The black rectangles represent the Geiger tubes and the region occupied by the magnetic field. These are in their full scale positions relative to the projected pictures. This arrangement allows a rapid preliminary survey of the pictures. Accidental tracks which obviously do not belong to each other in the paired pictures are discarded. Having made a preliminary survey, the numbers of the legitimately paired pictures are recorded.

Finally, each picture is projected onto a flat which may be rotated about a vertical axis. One meter from this axis is a scale marked every mm along a one meter arc. On this flat is a family of parallel lines. The flat is first rotated until the image of the vertical reference wire is made parallel to the family. The scale reading is recorded. The family is then made parallel to the track and the scale reading is again recorded. The difference of the scale readings is the inclination of the track with respect to the vertical. The difference between the inclinations found in the two chambers is the approximate angular deflection due to the magnetic field.

DISCUSSION OF ERRORS

The measurement of the momentum of each particle is subject to certain errors. These may be classified under two main headings. One considers all the factors that limit the precise measurement of a trajectory that was undisturbed by other than the magnetic field. The second considers the possibility of an alteration in the trajectory by other means.

An estimate of the nominal error in measuring the angular deflection of a trajectory shown in photographs of the two chambers is $\Delta\varphi \sim .003$ radians. This estimate includes the net effect of many factors such as chamber distortions, the overall process of photography, development, and projection for measurement, and the actual measurement itself. The main lack of resolution appeared to be due to one of the two chambers. This chamber yielded distortions of the same character independent of its position. Were both chambers of a quality equal to the best, it is felt that the nominal error in the deflection could have been halved.

The error in determining the deflection constant of the magnetic field is estimated at about 1%. The total error in momentum may then be computed from equation (4) which involves only the angular deflection and the deflection constant.

Let P be the momentum calculated by use of (4) from the measured deflection φ. Due to an error $\Delta\varphi$ in φ, the true momentum could actually lie in an interval bounded by

$$(6) \qquad P_1 = P\left[1 - \frac{\Delta\varphi}{eK}P\right]^{-1}$$

and

$$(7) \qquad P_2 = P\left[1 + \frac{\Delta\varphi}{eK}P\right]^{-1}$$

If we express P in units of energy (BeV), it is necessary to write .126 for eK in (6) and (7); this corresponds to the deflection constant $K = 4.2 \times 10^5$ gauss · cm which was used. A plot of P_1 and P_2 is given in Figure 4. Since the deflection constant is known relatively accurately, the uncertainty in P due to measurements on each particle trajectory is quite well represented in Figure 4. For example, it is shown in that figure that a particle measured as 15 BeV momentum might actually have a momentum somewhere between $P = 23.3$ BeV and $P = 11.05$ BeV. If we regard the useful limit of the instrument as being that at which the error in the measurement of φ is equal to φ, this limit corresponds to 42 BeV.

The second type of error mentioned is due to an alteration of a particle's actual trajectory by causes other than magnetic deflection. Such an alteration would be due to the scattering of the particle as it passed through the material between the two chambers. We treat this problem by answering the question, "What are the chances that a particle will scatter so as to yield a deflection corresponding to a momentum ς times greater than its true momentum, P?" That is, we compute the probability that a net deflection of amount $(\varsigma - 1)\varphi/\varsigma$ will result due to scattering alone.

It is first necessary to decide whether single, multiple, or intermediate scattering must be considered. Jånossy (7) gives a criteria by which one may determine the type of scattering involved. This requires the computation of $N\pi r^2$. Here N is the number of scattering nuclei per square centimeter presented to the incident particle. r is the impact parameter corresponding to a Rutherford scattering resulting in a deflection of amount $(\varsigma - 1)\varphi/\varsigma$. If this product is less than or equal to one, we have single scattering; if it is greater than one, we must consider intermediate or multiple scattering. The relationship between $(\varsigma - 1)\varphi/\varsigma$

and r is

$$(8) \qquad r = \frac{2 z e^2 \rho}{pc(\rho - 1)\varphi}$$

In (8) z is the atomic number of the scattering nucleus; e is the charge of an electron. (8) is written for particles moving with velocities close to c.

Substitution of (4) and (8) into the product $N\pi r^2$ gives

$$(9) \qquad N\pi r^2 = 4\pi N z^2 \left(\frac{\rho}{\rho-1}\right)^2 \left(\frac{e}{Kc}\right)^2$$

$$= 4\pi N z^2 r_0^2 \left(\frac{\rho}{\rho-1}\right)^2 \left(\frac{m_0 c^2}{Kec}\right)^2$$

Above m_0 and r_0 are the mass and classical radius of the electron respectively. For the apparatus used, $N = 1.08 \cdot 10^{23}$ cm^{-2} and $z \sim 10$; these values in (9) give

$$(10) \qquad N\pi r^2 = 1.8 \left(\frac{\rho}{\rho-1}\right)^2 \cdot 10^{-4}$$

For $\rho = 1.1$, the above product is 2.2×10^{-2}. Hence, for this and larger values of ρ, the problem is one of single scattering. (10) is the fraction of a square centimeter presented to an incident particle which will scatter this particle by an amount $(\rho - 1)\varphi/\rho$ or more. It is, therefore, the chance that this particle might be mistaken for one of momentum equal to or greater than ρP.

For $\rho = 1.1$, this chance is about one out of fifty. Hence, we conclude that one out of fifty particles could scatter so as to give a momentum incorrect to 10%. Only six out of a thousand will scatter so as to give a momentum in error to 20%. These conclusions apply independent of the momentum considered.

Reference to Figure 4 reveals that individual measurements on 98% of the particles with momenta up to 5 BeV are limited by scattering to an accuracy of 90%. Beyond 5 BeV the limitation is due to the inability to measure a deflection to better than 3 millradians. It might be stated that 266 out of the 330 particles considered had apparent momenta less than 5 BeV.

DISCUSSION OF RESULTS

A total of 330 cases are considered. 197 of these are positive particles, 132 are negative, and the sign of one particle could not be determined. These particles are enumerated in the order of increasing momentum in Table II.

The excess of positives divided by the total gives .2. This positive excess lies intermediate to the values reported by previous workers (see Table I). It is considerably higher than the average. This difference could be attributed to statistical error until the number of cases is increased.

If this large excess is not of statistical or instrumental* origin, it might be due to a unique selection characteristic of the device. That is, the present instrument differs from most single chamber types in that particles are received through a narrow and well defined aperture. The aperture defined by the two counters is $8.67 \times 10^{-2}\ \mathrm{cm}^2 \cdot$ steradians. Only a few particles inclined more than about 5 degrees with the vertical can be detected. If the positive excess of energetic particles is a function of the zenith angle of entry, this work is consistent with a larger excess for nearly vertical incidence.

A second major instrumental difference is the method of reducing the soft component. Single chamber techniques depend mostly on lead absorbers to limit the soft component. The present technique cuts out all particles with momenta less than .3 BeV by means of the magnetic field. Only parti-

---

* Instrumental errors could be due to a malalignment of the Geiger counters or of the illuminating beams. Such dissymmetries could favor the detection of positive or negative particles. An earlier run with an entirely independent setting of the counters and the lights considered $\sim$ 100 cases. These gave a positive excess of $\sim$ .2.

cles above 1.3 BeV "see" an aperture essentially equal to the no field aperture (see Figure 2).

It is interesting to note that those workers who used lead to filter the soft component obtained the highest positive excess values.

Figure 5 presents a block curve of the differential momentum spectrum of all particles. This is a plot of the number of particles found in each .5 BeV momentum interval. The smooth curve is derived from the slope of the integral spectrum* for the particles. It appears to represent fairly the gross trends of the block curve. The instrumental maximum occurs at about .85 BeV; the instrumental maxima of other workers are given in Table I.

Figure 6 is a plot of the differential spectrum on log-log coordinate paper. This indicates that the high energy portion ($P > 2.5$ BeV) of the spectrum is well approximated by a function of the form $I(P) \propto P^{-2.1}$. Beyond 2.5 BeV, the relative aperture of the instrument does not differ from unity by more than 3% (see Figure 2). Thus this power law is not subject to appreciable correction due to aperture effect. The power law exponent -2.1 is intermediate to those derived from the data of other workers (see Table I). The values listed for other experimenters are derived in most cases from a replotting of data presented in the journals. In some cases the determinations may have been crude due to the inaccuracies of transplanting data from the small figures of the publications. The comparison must be regarded as very approximate.

If the "tail" of the spectrum is to assume the form of a power law with the same exponent holding to infinite energies, the exponent must be

---

* The integral spectrum is a direct plot of the data in Table II.

less than -2. Otherwise the integral for the total energy carried by the radiation diverges. The results of the present work would be consistent with a power law behavior to infinite momenta. Several workers (see Table I) obtain data inconsistent with this possibility. It should be stated that a power law behavior with an exponent less than -2 is by no means a necessity. It is entirely possible that at some high momentum the character of the spectrum could change or cut off so as to give a convergent integral beyond this momentum. For lesser momenta any or no power law could hold.

Figure 7 is a plot of the differential spectra for the positive and the negative particles. These are shown in block form; they exhibit similar behavior in their gross trends.

There exists a probability that the few particles which show small deflections (and consequently appear to have large momenta) are in reality low momentum particles which have been scattered. The chance that a particle with true momentum P will scatter so as to yield an apparent momentum $P' = \rho P$ or greater is given by (10). Let us denote this by C ; whence

$$C = 1.8 \left(\frac{P'}{P'-P}\right)^2 \cdot 10^{-4} \tag{11}$$

If the true differential spectrum of the particles is $\frac{dN}{dP}$, then the number of particles between P_1 and P_2 ($P' > P_2 > P_1$) that will scatter into the range $\infty > P > P'$ is

$$\begin{aligned} n &= 1.8 \cdot 10^{-4} \int_{P_1}^{P_2} \left(\frac{P'}{P'-P}\right)^2 \left(\frac{dN}{dP}\right) dP \\ &= 1.8 \cdot 10^{-4} \int_{N_1}^{N_2} \left(\frac{P'}{P'-P}\right)^2 dN \end{aligned} \tag{12}$$

If we assume that the integral spectrum obtained is approximately correct, we may compute n from it. For example, 12 particles appeared to have momenta greater than 25 BeV. By use of (12) we compute that there is a chance that 1/10 of a particle from the remaining 318 with momenta less than 25 BeV could have been scattered in such a way as to be mistaken for one of the twelve. Indeed the scattering would have to be in a plane nearly normal to the magnetic field to be so interpreted; thus, the chances are even smaller.

We see from Figure 4 that a particle of 16 BeV momentum could be mistaken for a 25 BeV particle due to the error on measurement in φ. Particles with lesser momentum could not be misidentified as 25 BeV particles. Thus the existence of single particles with momenta and energy of 16 BeV is quite certain on the basis of these direct measurements. If the true spectrum cuts off at some momentum, this cut-off must be greater than 16 BeV.

The particles for which the spectra have been determined are most probably mesotrons. No heavily ionizing tracks were observed; so it is not likely that protons were present with momenta less than .7 BeV. This is the value of momentum below which it is possible to distinguish mesotrons and protons by specific ionization. The possibility of an appreciable electron component is slight as these particles tend to produce showers; only single particles were considered.

Rossi (8) states,

> "For the determination of the momentum spectrum of mesons at sea level from cloud chamber pictures of cosmic ray particles in magnetic fields, one is justified in considering as mesons all penetrating particles which cannot be shown to be different from mesons by their specific ionization."

REFERENCES

(1) C. D. Anderson and S. H. Neddermeyer, Int. Conf. Physics, London, (1934), 177

(2) L. Le Prince-Ringuet, J. de Phys. et Rad., (1937), 8, 207

(3) P. M. S. Blackett, Proc. Roy Soc., (1937), A159, 1

(4) H. Jones, Rev. Mod. Phys., (1939), 11, 235

(5) D. J. Hughes, Phys. Rev., (1940), 57, 592

(6) J. G. Wilson, Nature, (1946), 158, 415

(7) L. Jánossy, Cosmic Rays, Oxford Press, (1948), 98

(8) B. Rossi, Rev. Mod. Phys., (1948), 20, 537

APPENDIX A

THE APERTURE OF THE INSTRUMENT

It has been mentioned that the presence of the magnetic field introduces selective properties into the instrument. Particles with lower than a critical momentum are completely excluded from detection. Particles with higher momenta are received through a smaller effective aperture. This selectivity is, of course, an instrumental bias which must be removed in the final accounting of the data.

Figure 8 presents a series of sketches which illustrate the effect of the magnetic field on particles of different momenta or radii of curvature ρ. Figure 8(a) shows the trajectory of a particle with the minimum radius ρ_0. Particles with a lesser radius cannot be detected; hence ρ_0 is a "cut-off" value for ρ.

Sketches 8(b), 8(c), 8(d) describe particles of radius somewhat greater than ρ_0. It is evident that such particles can penetrate the top counter in a limited region and be detected. Let x be the distance from the left end of the top counter and the point of penetration as shown in 8(c). x may assume values between zero (see 8(b)) and ξ. ξ is the maximum value of x possible for particles with the radius considered (see 8(d)). Also indicated is the angle, $\Delta\theta_1$, between the extreme directions of entry at a station x. 8(c) shows the nature of the limitations imposed on the angles of entry, θ_1, at each station x.

Figures 8(e), 8(f), and 8(g) demonstrate the behavior of particles with a radius ρ_1. A particle with this particular radius enters the top counter vertically at its left end and emerges from the right end of the bottom counter (see 8(g)). The geometrical constraints limiting θ_1 have the same character for ρ between ρ_0 and ρ_1 .

For ρ greater than ρ_1 , a different type of constraint is imposed on θ_1 . Some typical trajectories for particles with such a radius are shown in 8(h), 8(i), 8(j), 8(k), and 8(l). For x between zero and a , the extremities of the bottom counter indirectly limit θ_1 (see 8(h), 8(i), 8(j)). At $x = a$, a particle entering with a maximum θ_1 , emerges vertically from the left end of the bottom counter (see 8(j)). For x greater than a , the limitations on θ_1 resume the form imposed on particles with $\rho_0 < \rho < \rho_1$ (see 8(j), 8(k), 8(l)).

Figure 8(m) shows the behavior of particles with an infinite radius of curvature.

The integration of equation (1) with respect to dA and $d\Omega$ is carried out over the top counter. Referring to the dimensions shown on Figure 1, dA and $d\Omega$ are given by

$$(13) \quad dA = T\,dx$$

$$(14) \quad d\Omega = \frac{T}{D} \Delta\theta_1$$

$\Delta\theta_1$ is given as a function of x below the sketches of Figure 8. The dependence given applies to the class of radii pictured in the accompanying sketch. Also, the limits within which x may vary are written on Figure 8. $\Delta\theta_1$ and the limits on x are computed from the first order approximations of some rigorous equations. Quantities of order θ_1^2 and higher were neglected in reducing the precise equations.

The aperture integral is

$$(15) \quad \int dA\,d\Omega = \int_{x_1}^{x_2} \frac{T^2}{D} \Delta\theta_1\,dx$$

Above x_1 and x_2 are the appropriate limits of integration for any particular momentum or radius considered. The relative aperture, $\frac{1}{\gamma}$ is obtained on dividing (15) by $\left(\frac{WT}{D}\right)^2$ which is the no-field aperture for all particles. The results of the computation for $\frac{1}{\gamma}$ are presented below.

(16) For $\rho_0 \leq \rho \leq \rho_1$

$$\frac{1}{\gamma} = \frac{1}{6\epsilon^2}\left(\frac{\rho_1}{\rho}\right)^2(\eta-1)^2(2\eta+1)$$

and (17) For $\rho_1 \leq \rho \leq \infty$

$$\frac{1}{\gamma} = 1 - \frac{1}{6}(3-2\epsilon)\left(\frac{\rho_1}{\rho}\right)^2$$

The quantities ϵ, ρ_0, ρ_1, and η are defined by

(18) $$\epsilon = \frac{L}{D}$$

(19) $$\rho_0 = \frac{L(2D-L)}{8W}$$

(20) $$\rho_1 = \frac{DL}{2W}$$

(21) $$\eta^2 = 1 + 2\epsilon\left(2\frac{\rho}{\rho_1} - 1\right) + \epsilon^2$$

The following properties of equations (16) and (17) are noted:

(a) $\frac{1}{\gamma} \to 0$ as $\rho \to \rho_0$

(b) $\frac{1}{\gamma} = \frac{1}{2} + \frac{1}{3}\epsilon$ for $\rho = \rho_1$

(c) $\frac{1}{\gamma} \to 1$ as $\rho \to \infty$

(d) $\dfrac{d\left(\frac{1}{\gamma}\right)}{d\left(\frac{\rho}{\rho_1}\right)} = 0$ for $\rho = \rho_0$ and $\rho \to \infty$

(e) The slopes of the equations (16) and (17) are equal at the point ($\rho = \rho_1$) separating their regions of applicability. This is

$$\frac{d\left(\frac{1}{\gamma}\right)}{d\left(\frac{\rho}{\rho_1}\right)} = 1 - \frac{2}{3}\epsilon$$

Figure 2 is a plot of the relative aperture computed by inserting the dimensions of Figure 1 into (16) and (17).

It may be noted that the equations for $\frac{1}{\gamma}$ assume a simple form for $L = D$. That is, for the case of the counters placed directly above and below the field. This corresponds to the maximum attainable aperture. The equations, of course, are valid only when the vertical length of the field is much greater than its width and breadth.

APPENDIX B

DERIVATION OF THE MOMENTUM FROM THE DEFLECTION AND DETERMINATION OF THE DEFLECTION CONSTANT

The momenta of the particles are determined from their observed deflections caused by a magnetic field. It is assumed that the field is unidirectional; that is, everywhere parallel to a horizontal line. It is further assumed that the field strength is solely a function of a vertical space coordinate. The field has been explored by Mr. Donald Glaser, and this assumed behavior was found to be approximately correct. Under these conditions, the magnitude of field strength at a depth ℓ below a datum level may be expressed as $B(\ell)$. Figure (9) shows a particle of momentum P and charge e moving in a plane normal to such a field.

The field above and below the two dotted lines is zero; thus the particle trajectory in these regions is rectilinear. Let θ be the angle between the direction of motion at depth ℓ and the vertical as shown in the figure; θ_1 and θ_2 being the values assumed by θ in the regions void of magnetic field. The radius of curvature, ρ, of the trajectory at depth ℓ is given by

$$\frac{1}{\rho} = \frac{e}{P} B(\ell) \qquad (22)$$

but

$$\frac{1}{\rho} = -\frac{d\theta}{ds} = -\frac{d\theta}{d\ell}\cos\theta \qquad (23)$$

Substituting (23) in (22), there results

$$-\cos\theta \, d\theta = \frac{e}{P} B(\ell) \, d\ell$$

and $\int_{\theta_1}^{\theta_2} -\cos\theta \, d\theta = \sin\theta_1 - \sin\theta_2 = \frac{e}{p} \int B(l)\,dl$

Solution of the above for $\frac{p}{e}$ yields

$$\frac{p}{e} = \frac{\int B(l)\,dl}{\sin\theta_1 - \sin\theta_2}$$

or (24) $$\frac{p}{e} = \frac{K}{\sin\theta_1 - \sin\theta_2}$$

where $$K = \int B(l)\,dl$$

K, the "deflection constant" of the field, has the units of gauss centimeters in the e.m.u. system. Thus the momentum or magnetic curvature of a particle is directly calculable from θ_1, θ_2 and the deflection constant K. θ_1 and θ_2 are obtained from the cloud chamber photographs.

K is a function of the magnetic field strength and hence depends upon the magnet current, I, which produces the field. $K(I)$ could be determined from a complete knowledge of the magnetic field strength as it depends on l for each value of I. However, it is the integral of the magnetic field that is of interest here, rather than a detailed knowledge of its distribution. The following technique is devised to determine this integral.

First it is noted that a perfectly flexible wire carrying a current i and under tension T assumes a radius of curvature ρ such that

(25) $$\frac{1}{\rho} = \frac{i}{T} B(l)$$

But (25) is precisely equation (22) with the ratio $\frac{i}{T}$ appearing in place of $\frac{e}{p}$. Hence it is evident that if such a wire enters the magnetic field at an angle θ_1 and emerges at an angle θ_2, the deflection constant of the field may be obtained by means of

$$K(I) = \frac{T}{i}(\sin\theta_1 - \sin\theta_2) \tag{26}$$

An actual determination of $K(I)$ is made using the arrangement shown in Figure 10.

A current, i, is made to flow through the thin wire circuit ABCD. Points A and D are held fixed. Weights, W, are hung at points C and B. The branch $\overline{BC}$ is loosely coiled wire; the branches $\overline{AB}$ and $\overline{DC}$ thus emerge vertically from the magnetic field. The arrangement yields data for two determinations of the deflection constant, one for each branch, $\overline{AB}$ and $\overline{DC}$. The angles θ_1 and θ_1' are measured from photographs.

The above technique neglects the mass and rigidity of the wire. The mass of the wire is one-thousandths part of W. The change in internal stress energy of the wire due to its curvature is computed. This is found to be less than one forty-thousandths of the change in potential energy of W as the current is increased from zero to i. Thus the assumptions of a massless and perfectly flexible wire are not unreasonable.

Copper wire .005 inch in diameter is used in the experiment. W is 100 grams; i is about .03 amperes.

The arithmetic mean of the two determinations of $K(I)$ is plotted as a function of I in Figure 11. A separate ordinate scale shows an effective average magnetic field. This is obtained by dividing K by 40 centimeters, the vertical length of the pole faces. The curve, as expected, has the form of the "knee" of a hysteresis curve. If the error in K is measured in terms of the dispersion of points about the curve, this error is about 1% in the region above the "knee". It is estimated that the greatest source of error in the determination of κ is due to the measurement of θ_1 from the photographs.

It should be mentioned that the technique is suitable for the determination of magnetic field strengths in other apparatus. Where the cloud chamber is immersed in a magnetic field, the actual curvature of the wire may be photographed and measured.* In all cases, the desired information is obtained from a "sample particle trajectory" in the form of a wire carrying a known current and under a known tension.

---

* This has been done by R. V. Adams for a one-chamber instrument with results in good agreement with other techniques.

APPENDIX C

MEASUREMENT OF THE DEFLECTION FROM PHOTOGRAPHS

The particle shown in Figure 1 moves in a helical path through the region of the approximately uniform magnetic field. Let a rectangular coordinate system be centered at the point of the particle's entry into this field. The z axis is taken along the direction of the field; in Figure 12, this axis is normal to the plane of the paper.

The x and y axes are oriented horizontally and vertically respectively as shown in the figure. The equations of the helix are

$$x = \rho\,[\cos\theta - \cos\theta_1] \tag{27}$$

$$y = \rho\,[\sin\theta_1 - \sin\theta] \tag{28}$$

$$z = [v \sin\delta] \cdot t \tag{29}$$

In the above, ρ is the radius of the cylindrical surface containing the helix. v is the speed of the particle. t is the time measured from the instant of entry into the field. $v \sin\delta$ is the component of v along the direction of the field; thus δ is the pitch angle of the helix. θ , as before, is the angle between the tangent to the projected curve (projected on xy plane) and the y axis. θ and t are related according to

(30 $$\theta = \theta_1 - \frac{v\cos\delta}{\rho}\, t$$

The inclination of the trajectory with the xy plane is measured by

$$\frac{dz}{dy} = \frac{\tan\delta}{\cos\theta} \tag{31}$$

Since θ is small, $\frac{dz}{dy}$ is given approximately by

$$(32) \qquad \frac{dz}{dy} \cong \tan\delta$$

Thus the trajectories of the particles detected are very nearly plane curves. The planes are parallel to the x axis. The angle between a trajectory plane and the xy plane is δ , the pitch angle of the helix.

In the experiment performed, it is the component of a particle's momentum parallel to the xy plane which is determined. θ_1 and θ_2 may be determined from photographs of the particle's trajectory in the two cloud chambers. θ_1 and θ_2 are then substituted into equation (24) to compute the desired momentum component. The total momentum is obtained by dividing this component by $\cos\delta$. Since δ cannot exceed $2.0 \cdot 10^{-2}$ radians (see Figure 1), the total momentum cannot differ by more than $2.0 \cdot 10^{-2}$ percent from the computed component.

Each cloud chamber is photographed by a pair of identical cameras. The cameras are held fixed with their films coplanar; the common plane being perpendicular to the magnetic field. All four cameras photograph a thin wire held vertically. The image of this wire establishes a true vertical reference on each film.

θ_1 is determined from a pair of photographs of the top cloud chamber. The "pinhole" camera image of a straight line is the intersection of a plane determined by the line and the "pinhole" with the plane of the camera's film. The actual angle measured in each photograph is that between the images of the fine vertical reference wire and of the track (see Figure 3). The angle of interest, θ_1 , is that between the projections of the vertical wire and the track upon the film. The measured angle and the desired angle are not generally the same. This is due to the two distinct methods of generating the directions in space - one by pinhole photography (i.e., projecting through a point) and the other by direct perpendicular projection onto a plane.

In any case we are interested in comparing angles between directed lines established by different constructions. A common feature of the two constructions is that each involves the intersections of certain planes with the film plane. A second feature in common is that all of the planes which intersect the film plane contain the track. As far as establishing directions in space we may as well consider the intersections in a plane (plane P in Figure 13(a)) parallel to the film and passing through the front nodal points of the two cameras.

Let us denote these nodal points as O_1 and O_2 (see Figure 13(a)). Let T be the point of intersection of the extended track with plane P. Line $\overline{TV}$ is the intersection of a vertical plane through the track with plane P. Line $\overline{TD}$ is the intersection of the plane through the track with P which is normal to P.

The desired angle, θ_1, is

$$\theta_1 = \angle VTD$$

The angles we measure on the film are

$$\psi_1 = \angle VTO_1$$

and

$$\psi_2 = \angle VTO_2$$

If S be the distance $\overline{O_1 O_2}$, then it is easily shown (see Figure 13(b)) that

$$(33) \qquad \theta_1 = \psi_1 + \tan^{-1}\left[\frac{\delta_1}{S}\cdot\frac{\sin(\psi_1 - \psi_2)}{\cos\psi_2}\right]$$

$$\text{or } (34) \qquad \theta_1 = \psi_2 + \tan^{-1}\left[\frac{\delta_2}{S}\cdot\frac{\sin(\psi_1 - \psi_2)}{\cos\psi_1}\right]$$

In (33) and (34) $\delta_1 = \overline{O_1 Q_1}$ and $\delta_2 = \overline{O_2 Q_2}$. Q_1 is the point of intersection of a line through O_1 and normal to $\overline{TO_1}$ with $\overline{TD}$. Q_2 is a similar point for camera O_2. (33) and (34) would provide two means of measuring θ_1 in terms of available angles and distances if δ_1 and δ_2 could be established.

If ϵ_1, ϵ_2 are the distances of closest approach of the image of the track to the film centers and f is the distance from the nodal points to the film, then

$$(35) \qquad \theta_1 = \psi_1 + \tan^{-1}\left[\frac{\epsilon_1 \mathcal{L}_1}{f S}\cdot\frac{\sin(\psi_1 - \psi_2)}{\cos\psi_2}\right]$$

$$\text{or } (36) \qquad \theta_1 = \psi_2 + \tan^{-1}\left[\frac{\epsilon_2 \mathcal{L}_2}{f S}\cdot\frac{\sin(\psi_1 - \psi_2)}{\cos\psi_1}\right]$$

$\overline{Q_1 Z_1}$ and $\overline{Q_2 Z_2}$ are perpendicular to P; Z_1, Z_2 are the points of the track intersected by $\overline{Q_1 Z_1}$, $\overline{Q_2 Z_2}$. In the above

$$\mathcal{L}_1 = \overline{Q_1 Z_1}$$

$$\mathcal{L}_2 = \overline{Q_2 Z_2}$$

It is noted that ψ_1 and ϵ_1 are observable from film ①; ψ_2, ϵ_2 are observable from film ②. $\mathcal{L}_1$ or $\mathcal{L}_2$ may be obtained by utilizing data from both films simultaneously (such as by stereoscopic projection).

f and S are constants.

Let the pictures be projected through the same lenses used in photography. The film is f distant from the rear nodal points and the screen is $\mathcal{L}_0$ distant from the front nodal points of the lenses. Then the distances $\delta_{o_{1,2}}$ of closest approach of the two projected track images are

$$\delta_{o_1} = \frac{\mathcal{L}_o}{\mathcal{L}_1} \delta_1$$

$$\delta_{o_2} = \frac{\mathcal{L}_o}{\mathcal{L}_2} \delta_2$$

The error introduced in θ_1 by using δ_{o_1} in (33) instead of δ_1 is found by taking the differential of θ_1 in (33). This is evaluated under the most pessimistic conditions; it is $d\theta_1 \sim 10^{-5}$ radians. Hence one is completely justified in using δ_{o_1} for δ_1 in (33). This means that simple projection of each camera's picture will provide ample data to determine θ_1 to 10^{-5} radians. The necessary data are Ψ_1 , Ψ_2 , δ_{o_1} and S .

The error in equating θ_1 to Ψ_1 is found from (33). This evaluated under the most pessimistic conditions is .0015 radians. This may be ignored until cloud chambers with lesser distortion are available.

DATE, WORKERS AND REFERENCE	RESOLVING POWER (BeV)	NUMBER OF CASES CONSIDERED	INSTRUMENTAL MAXIMUM OF DIFFERENTIAL SPECTRUM (BeV)	APPROXIMATE POWER LAW EXPONENT FOR HIGH MOMENTA	POSITIVE EXCESS	MEANS OF LIMITING SOFT COMPONENT
1934 ANDERSON AND NEDDERMEYER (1)	~ 5	78	~ .85	-1.7	.08	----
1937 LE PRINCE-RINGUET (2)	~ 20	~ 300	~ 1.0	---	.26	Lead
1937 BLACKETT (3)	~ 20	~ 800	~ .85	-1.9	.07	----
1939 JONES (4)	~ 10	923	~ .9	-1.9	.13	Lead
1940 HUGHES (5)	~ 16	674	~ 1.0	-2.5	.1	Lead
1946 WILSON (6)	~ 20	~ 600	~ .75	-1.8	---	Lead
1949 (PRESENT WORK)	~ 40	330	~ .85	-2.1	.2	Strong Magnetic Cut-off

TABLE I

TABLE II

ENUMERATION OF PARTICLES IN THE ORDER OF INCREASING MOMENTUM

PARTICLE NUMBER	MOMENTUM (BeV)	SIGN
1	.351	-
2	.390	-
3	.423	-
4	.438	+
5	.490	-
6	.500	-
7	.532	-
8	.540	+
9	.543	-
10	.560	-
11	.578	+
12	.600	+
13	.600	-
14	.606	+
15	.610	+
16	.630	+
17	.640	-
18	.643	+
19	.647	+
20	.650	-
21	.657	+
22	.663	-
23	.667	-
24	.674	+
25	.674	+
26	.680	-
27	.700	-
28	.703	+
29	.729	+
30	.732	-
31	.732	-
32	.740	+
33	.758	+
34	.764	+
35	.764	-
36	.764	-
37	.773	+
38	.773	+
39	.783	+
40	.792	+
41	.823	+
42	.828	+
43	.835	-
44	.845	-
45	.857	-
46	.863	-
47	.868	+
48	.876	-
49	.881	-
50	.887	+
51	.893	+
52	.893	+
53	.906	-
54	.906	-
55	.919	+
56	.940	+
57	.948	+
58	.962	-
59	.985	+
60	.990	+
61	1.01	+
62	1.02	+
63	1.03	-
64	1.06	+
65	1.07	+
66	1.07	-
67	1.10	+
68	1.10	-
69	1.11	+
70	1.11	+
71	1.11	+
72	1.11	-
73	1.12	-
74	1.14	+
75	1.14	+
76	1.15	+
77	1.18	-
78	1.18	-
79	1.20	-
80	1.20	-
81	1.21	+
82	1.22	+
83	1.24	+
84	1.24	+
85	1.24	-
86	1.25	+
87	1.26	+
88	1.26	+
89	1.26	+
90	1.26	-
91	1.30	+
92	1.30	-
93	1.33	-
94	1.33	-
95	1.33	-
96	1.34	+
97	1.34	+
98	1.34	+
99	1.34	+
100	1.34	-

TABLE II (continued)

PARTICLE NUMBER	MOMENTUM (BeV)	SIGN
101	1.34	-
102	1.34	-
103	1.37	+
104	1.38	+
105	1.38	+
106	1.40	+
107	1.40	+
108	1.40	-
109	1.42	+
110	1.42	-
111	1.43	+
112	1.43	-
113	1.45	+
114	1.46	+
115	1.46	+
116	1.48	+
117	1.48	+
118	1.52	+
119	1.52	+
120	1.52	+
121	1.54	+
122	1.57	+
123	1.57	-
124	1.60	-
125	1.62	+
126	1.64	+
127	1.66	+
128	1.68	+
129	1.70	+
130	1.70	-
131	1.75	+
132	1.77	+
133	1.77	+
134	1.77	+
135	1.77	-
136	1.83	+
137	1.83	+
138	1.83	-
139	1.83	-
140	1.85	+
141	1.85	+
142	1.85	-
143	1.85	-
144	1.88	+
145	1.88	+
146	1.88	-
147	1.91	-
148	1.94	+
149	1.94	+
150	1.94	-

PARTICLE NUMBER	MOMENTUM (BeV)	SIGN
151	1.97	+
152	1.97	+
153	1.97	+
154	1.97	-
155	2.00	+
156	2.00	+
157	2.00	+
158	2.00	+
159	2.00	+
160	2.00	-
161	2.00	-
162	2.03	-
163	2.03	-
164	2.06	+
165	2.06	-
166	2.10	+
167	2.14	+
168	2.14	+
169	2.21	+
170	2.21	+
171	2.21	+
172	2.21	-
173	2.21	-
174	2.29	+
175	2.29	+
176	2.33	+
177	2.38	+
178	2.38	-
179	2.38	-
180	2.43	+
181	2.47	+
182	2.47	-
183	2.47	-
184	2.52	+
185	2.52	+
186	2.52	+
187	2.57	+
188	2.57	+
189	2.57	+
190	2.57	+
191	2.57	+
192	2.57	+
193	2.62	+
194	2.62	+
195	2.62	-
196	2.62	-
197	2.62	-
198	2.68	+
199	2.68	+
200	2.68	+

TABLE II (continued)

PARTICLE NUMBER	MOMENTUM (BeV)	SIGN	PARTICLE NUMBER	MOMENTUM (BeV)	SIGN
201	2.68	-	251	4.20	-
202	2.68	-	252	4.35	+
203	2.68	-	253	4.35	+
204	2.74	+	254	4.35	+
205	2.74	-	255	4.35	-
206	2.80	-	256	4.50	+
207	2.80	-	257	4.67	+
208	2.80	-	258	4.67	-
209	2.93	+	259	4.85	+
210	2.93	-	260	4.85	+
211	3.00	+	261	4.85	-
212	3.00	+	262	5.0	+
213	3.07	+	263	5.0	+
214	3.07	+	264	5.0	+
215	3.07	-	265	5.0	-
216	3.15	+	266	5.0	-
217	315	+	267	5.2	-
218	3.15	-	268	5.2	-
219	3.15	-	269	5.7	+
220	3.23	+	270	5.7	-
221	3.32	+	271	5.7	-
222	3.32	+	272	6.0	+
223	3.32	+	273	6.0	+
224	3.32	-	274	6.0	+
225	3.41	+	275	6.3	+
226	3.41	+	276	6.3	+
227	3.41	-	277	6.3	-
228	3.41	-	278	6.6	-
229	3.50	+	279	6.6	-
230	3.50	-	280	6.6	-
231	3.50	-	281	6.6	-
232	3.60	+	282	7.0	-
233	3.60	+	283	7.4	+
234	3.60	+	284	7.4	-
235	3.60	-	285	7.9	+
236	3.60	-	286	7.9	+
237	3.71	+	287	7.9	+
238	3.71	+	288	7.9	+
239	3.71	-	289	7.9	+
240	3.71	-	290	7.9	-
241	3.82	-	291	8.4	+
242	3.82	-	292	8.4	+
243	3.94	+	293	8.4	-
244	3.94	+	294	9.0	-
245	4.07	+	295	9.7	+
246	4.07	+	296	9.7	+
247	4.07	+	297	9.7	-
248	4.07	-	298	10.5	-
249	4.20	+	299	11.5	+
250	4.20	+	300	11.5	+

TABLE II (continued)

PARTICLE NUMBER	MOMENTUM (BeV)	SIGN
301	11.5	-
302	13	+
303	13	+
304	13	+
305	13	+
306	13	-
307	14	+
308	14	+
309	14	+
310	14	-
311	14	-
312	16	+
313	16	+
314	16	-
315	18	+
316	18	+
317	18	-
318	18	-
319	25	+
320	25	+
321	25	+
322	25	+
323	25	-
324	32	-
325	42	+
326	42	-
327	42	-
328	$>$42	-
329	$>$42	+
330	$>$42	?

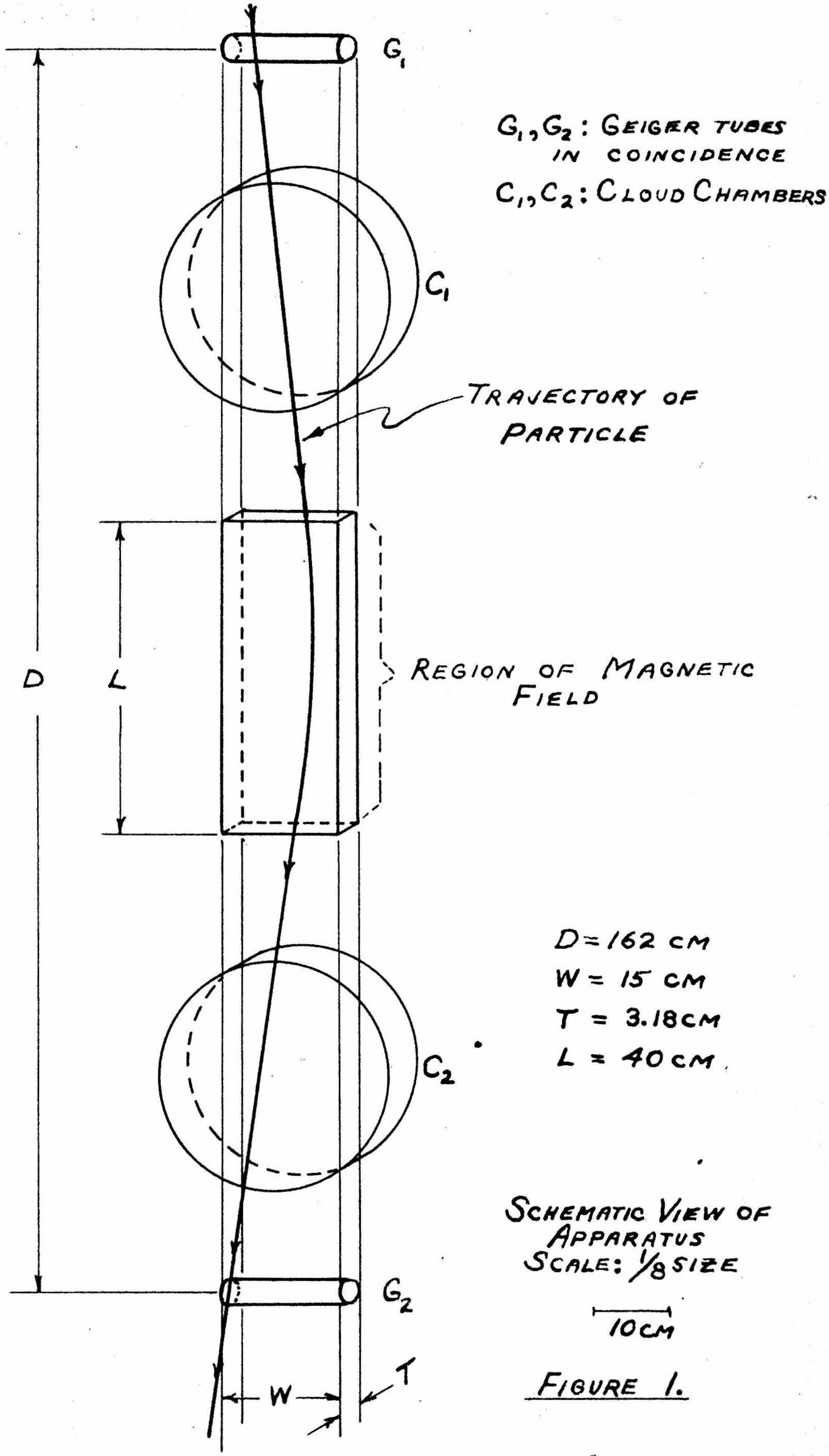
G1
G1, G2: Geiger tubes in coincidence
C1, C2: Cloud Chambers
C1
Trajectory of Particle
D
L
Region of Magnetic Field
D = 162 cm
W = 15 cm
T = 3.18 cm
L = 40 cm
C2
Schematic View of Apparatus
Scale: 1/8 size
10 cm
G2
W
T

FIGURE 1.

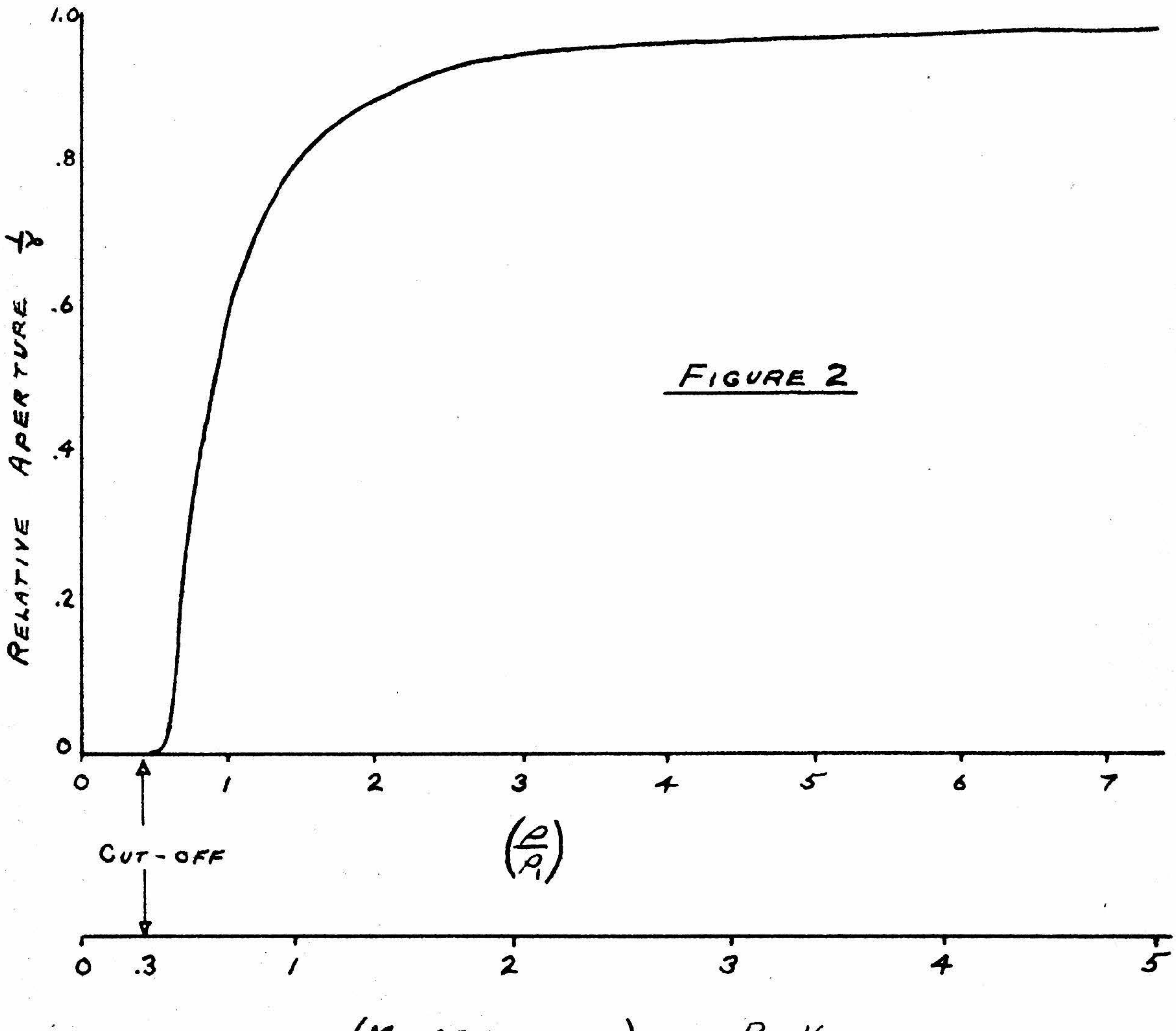

RELATIVE APERTURE $\left(\frac{1}{\gamma}\right)$ VS. MOMENTUM
(FOR MAGNET CURRENT = 75 AMPERES)

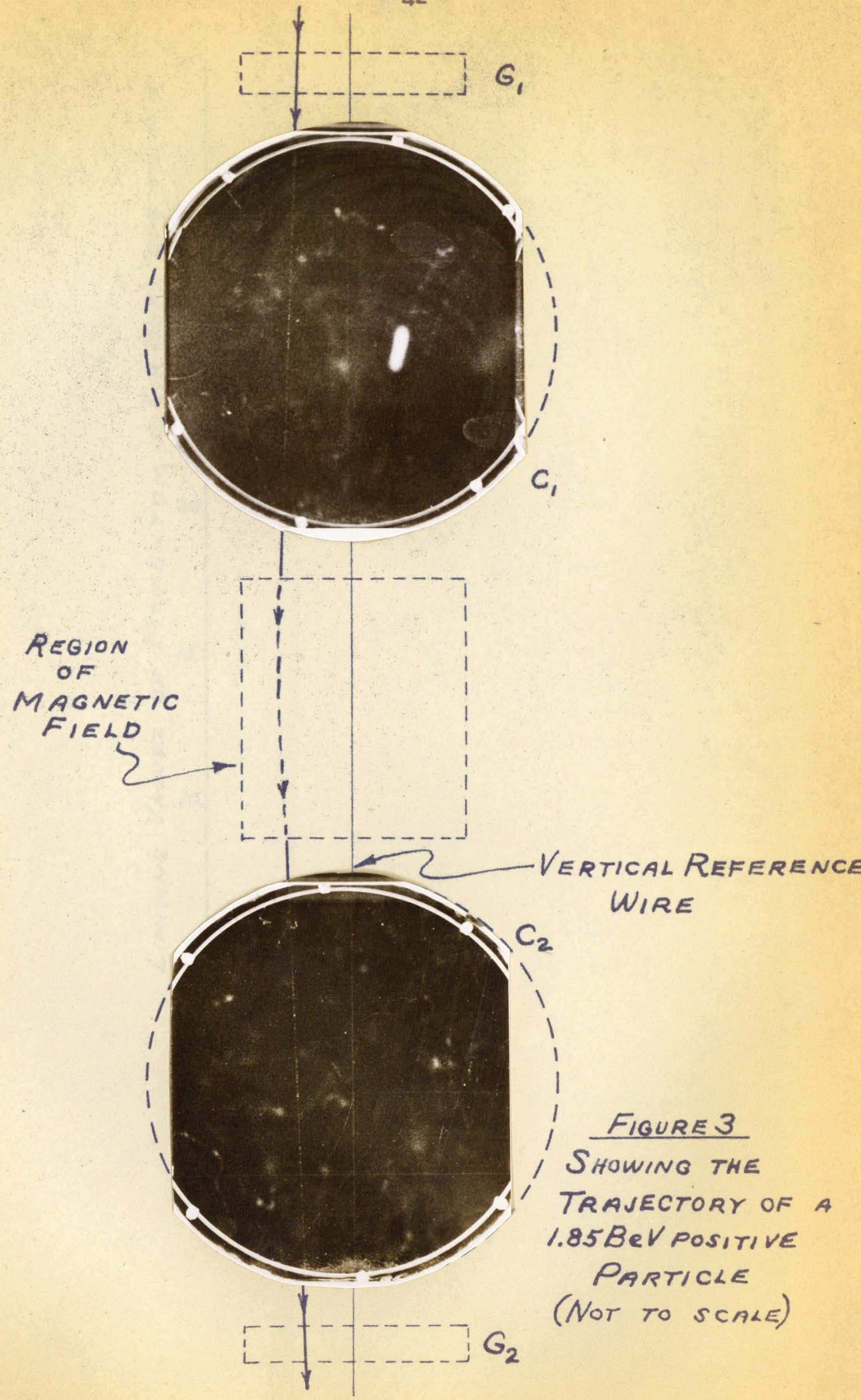

FIGURE 3
SHOWING THE TRAJECTORY OF A 1.85 BeV POSITIVE PARTICLE
(NOT TO SCALE)

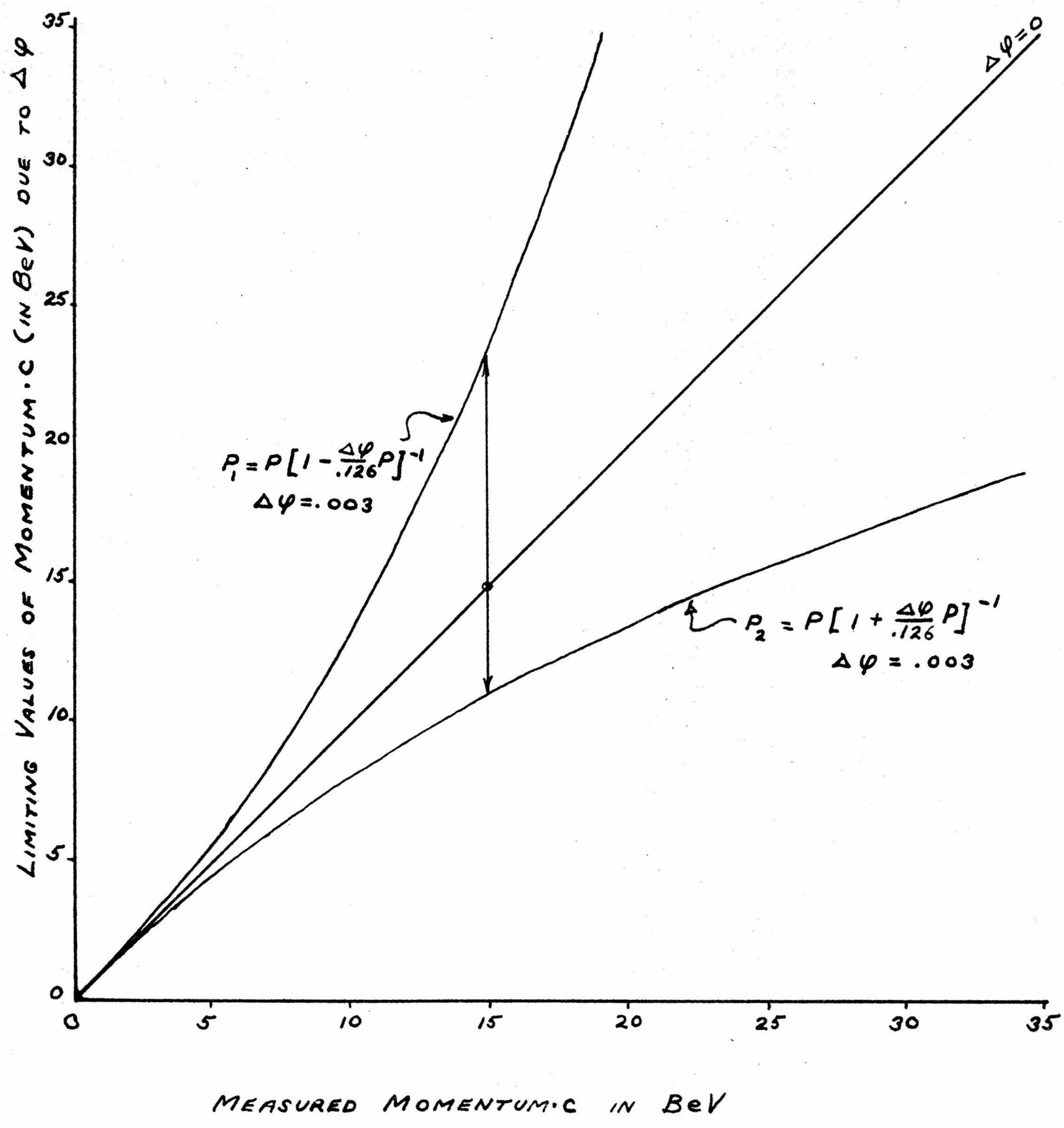
LIMITING VALUES OF MOMENTUM·C (IN BeV) DUE TO $\Delta\varphi$
MEASURED MOMENTUM·C IN BeV
$\Delta\varphi = 0$
$P_1 = P\left[1 - \frac{\Delta\varphi}{.126} P\right]^{-1}$
$\Delta\varphi = .003$
$P_2 = P\left[1 + \frac{\Delta\varphi}{.126} P\right]^{-1}$
$\Delta\varphi = .003$
0
5
10
15
20
25
30
35

FIGURE 4

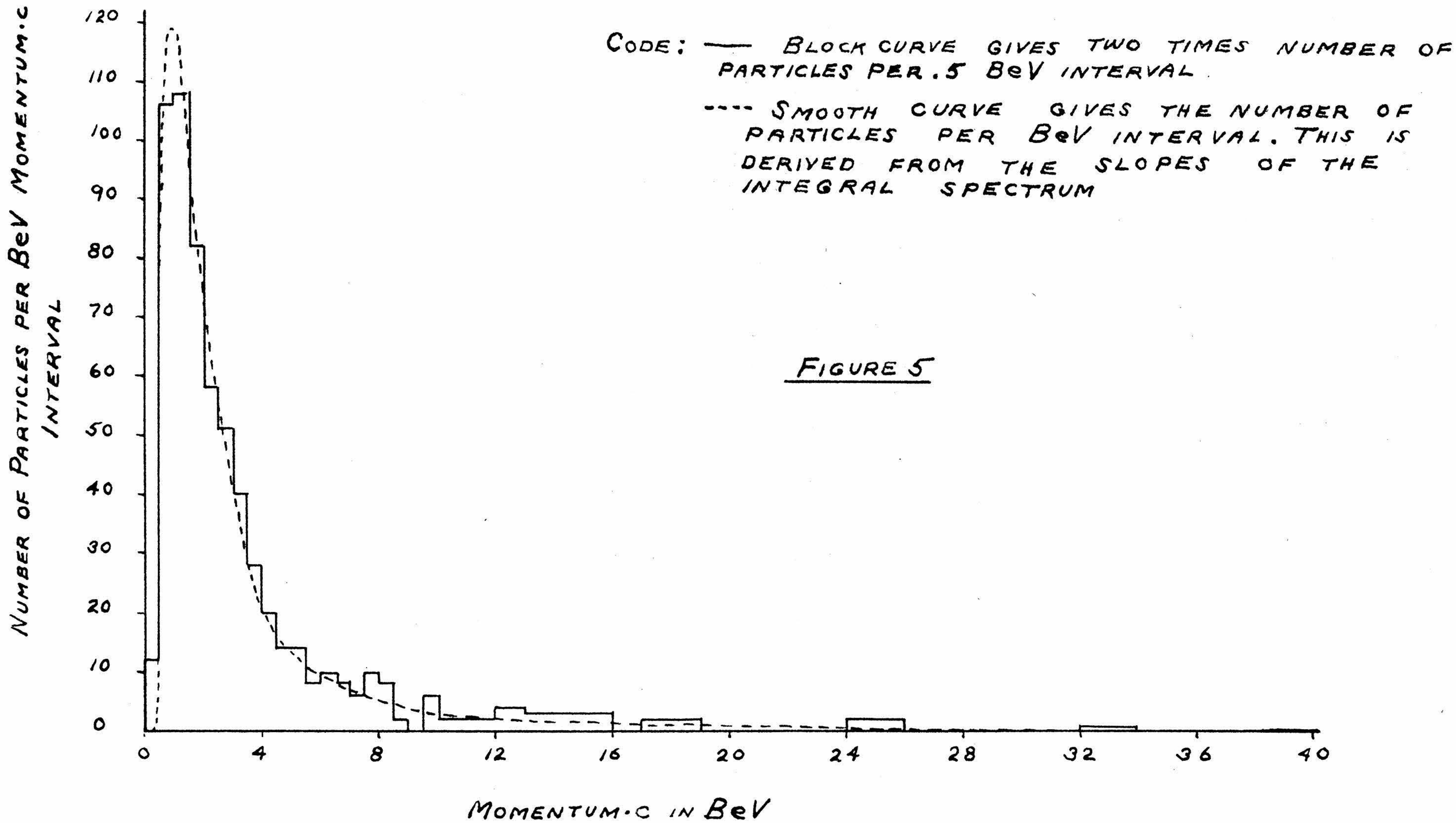

FIGURE 5

DIFFERENTIAL MOMENTUM SPECTRUM FOR ALL PARTICLES

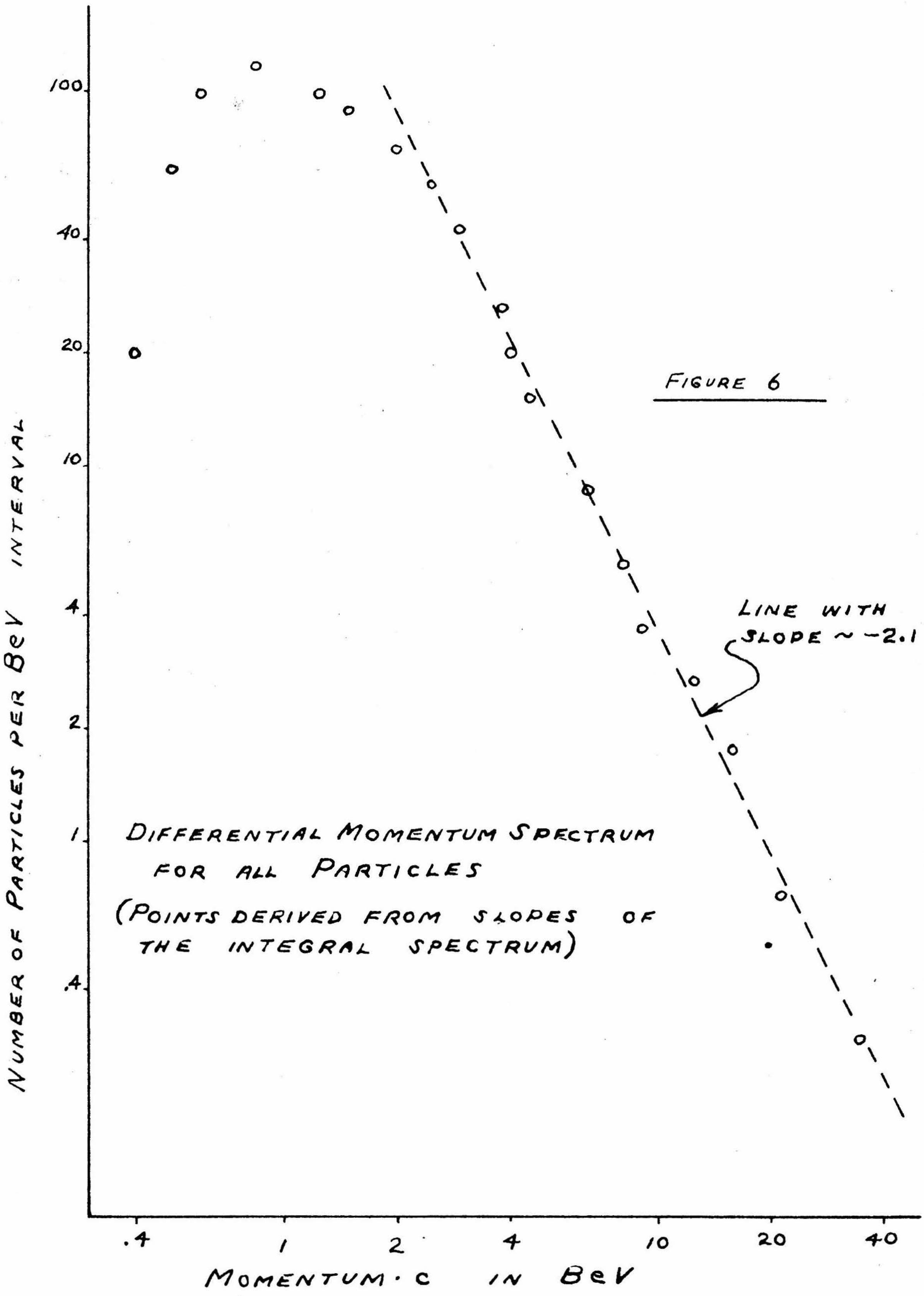
FIGURE 6
100
40
20
10
4
2
1
.4
.4
1
2
4
10
20
40
MOMENTUM · c IN BeV
NUMBER OF PARTICLES PER BeV INTERVAL
LINE WITH SLOPE ~ -2.1
DIFFERENTIAL MOMENTUM SPECTRUM FOR ALL PARTICLES
(POINTS DERIVED FROM SLOPES OF THE INTEGRAL SPECTRUM)

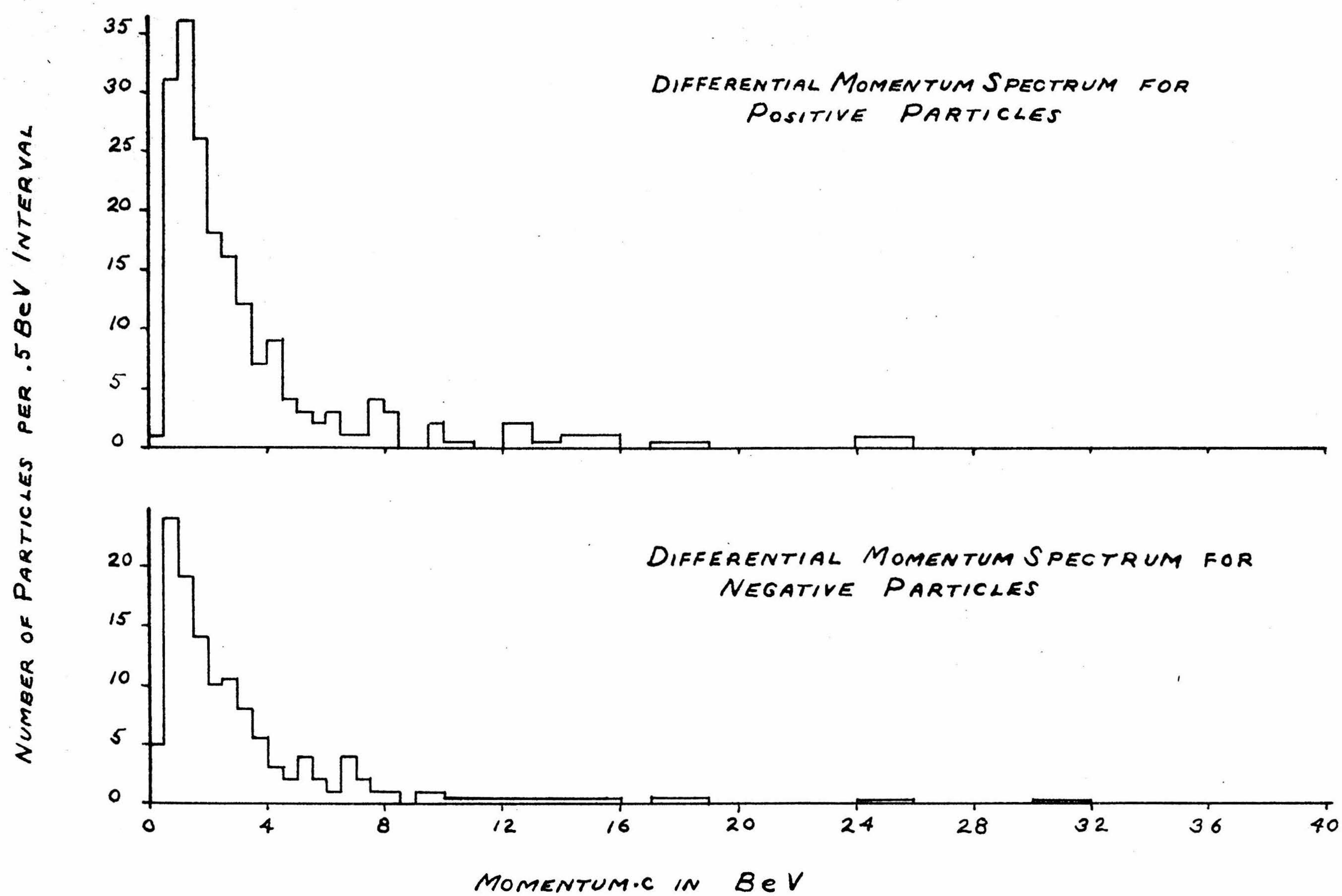

DIFFERENTIAL MOMENTUM SPECTRUM FOR POSITIVE PARTICLES
DIFFERENTIAL MOMENTUM SPECTRUM FOR NEGATIVE PARTICLES
NUMBER OF PARTICLES PER .5 BeV INTERVAL
0
5
10
15
20
25
30
35
0
4
8
12
16
20
24
28
32
36
40
MOMENTUM·C IN BeV

FIGURE 7

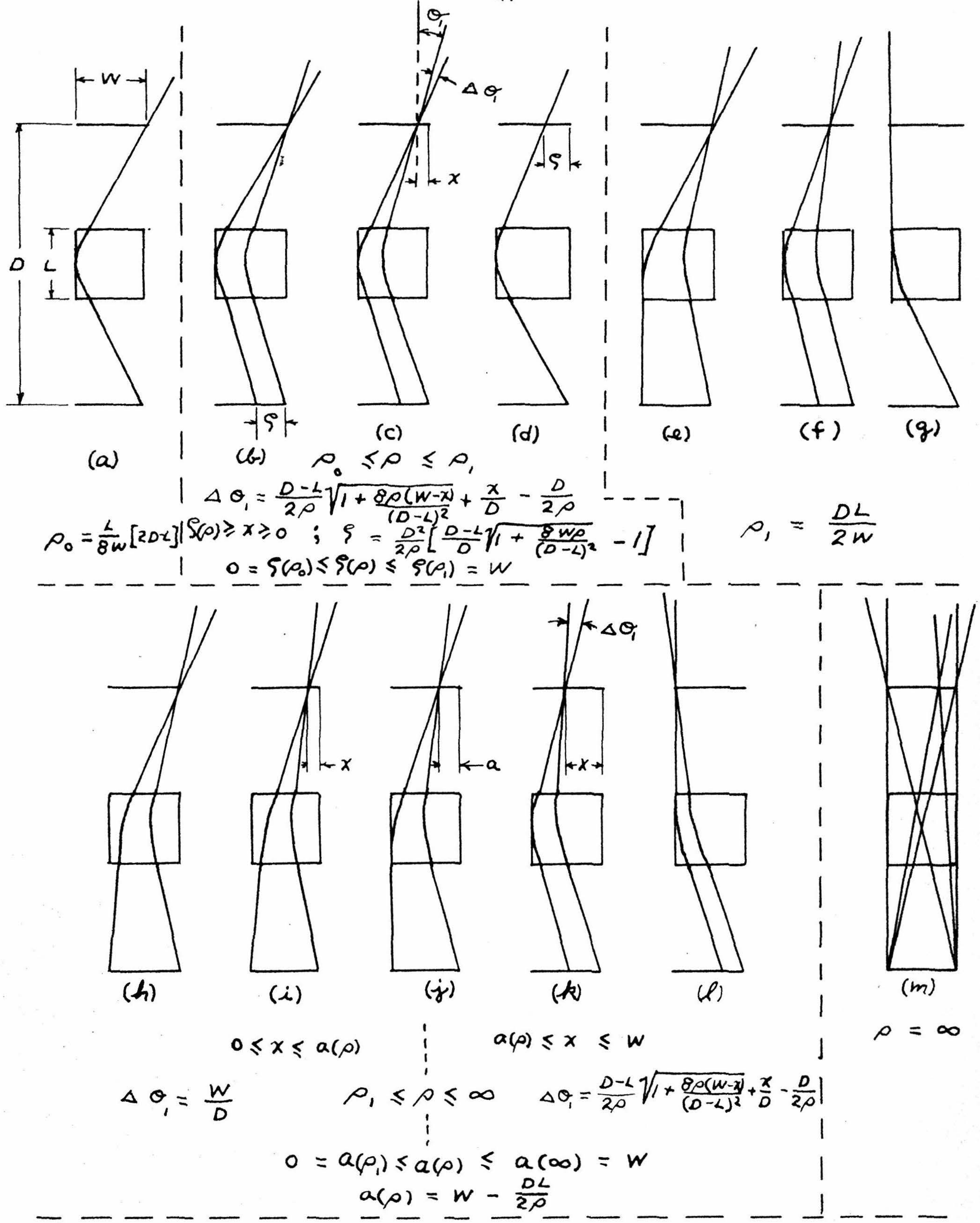

W
D
L
θ_1
$\Delta\theta_1$
x
ς
(a)
(b)
(c)
(d)
(e)
(f)
(g)
$\rho_0 \leq \rho \leq \rho_1$
$\Delta\theta_1 = \frac{D-L}{2\rho}\sqrt{1+\frac{8\rho(W-x)}{(D-L)^2}} + \frac{x}{D} - \frac{D}{2\rho}$
$\rho_0 = \frac{L}{8W}[2D-L]$
$\varsigma(\rho) \geq x \geq 0 \quad ; \quad \varsigma = \frac{D^2}{2\rho}\left[\frac{D-L}{D}\sqrt{1+\frac{8W\rho}{(D-L)^2}} - 1\right]$
$0 = \varsigma(\rho_0) \leq \varsigma(\rho) \leq \varsigma(\rho_1) = W$
$\rho_1 = \frac{DL}{2W}$
x
a
$\Delta\theta_1$
(h)
(i)
(j)
(k)
(l)
(m)
$0 \leq x \leq a(\rho)$
$a(\rho) \leq x \leq W$
$\rho = \infty$
$\Delta\theta_1 = \frac{W}{D}$
$\rho_1 \leq \rho \leq \infty$
$\Delta\theta_1 = \frac{D-L}{2\rho}\sqrt{1+\frac{8\rho(W-x)}{(D-L)^2}} + \frac{x}{D} - \frac{D}{2\rho}$
$0 = a(\rho_1) \leq a(\rho) \leq a(\infty) = W$
$a(\rho) = W - \frac{DL}{2\rho}$

FIGURE (8)

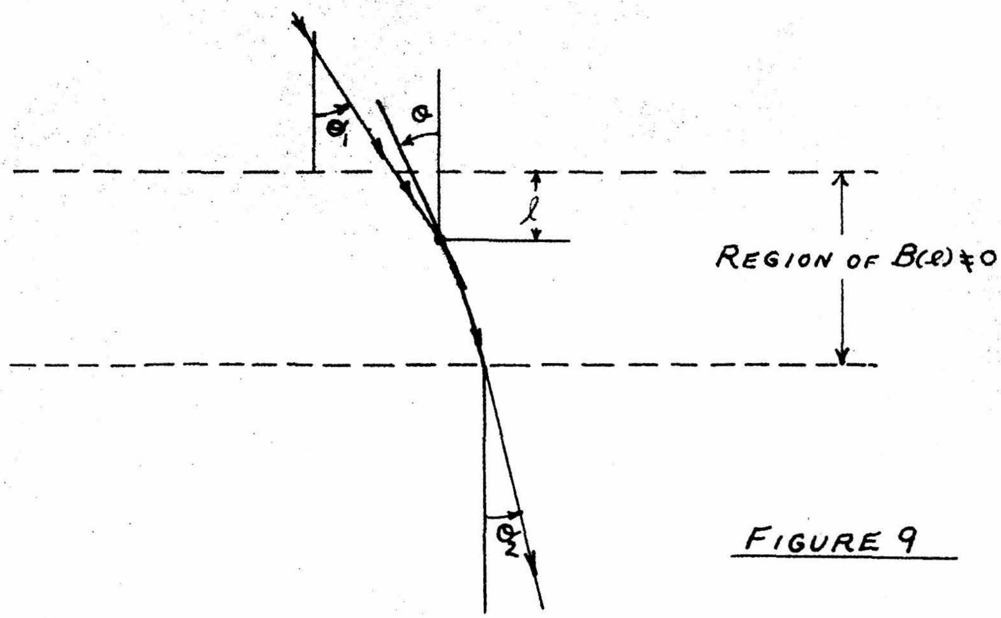

FIGURE 9

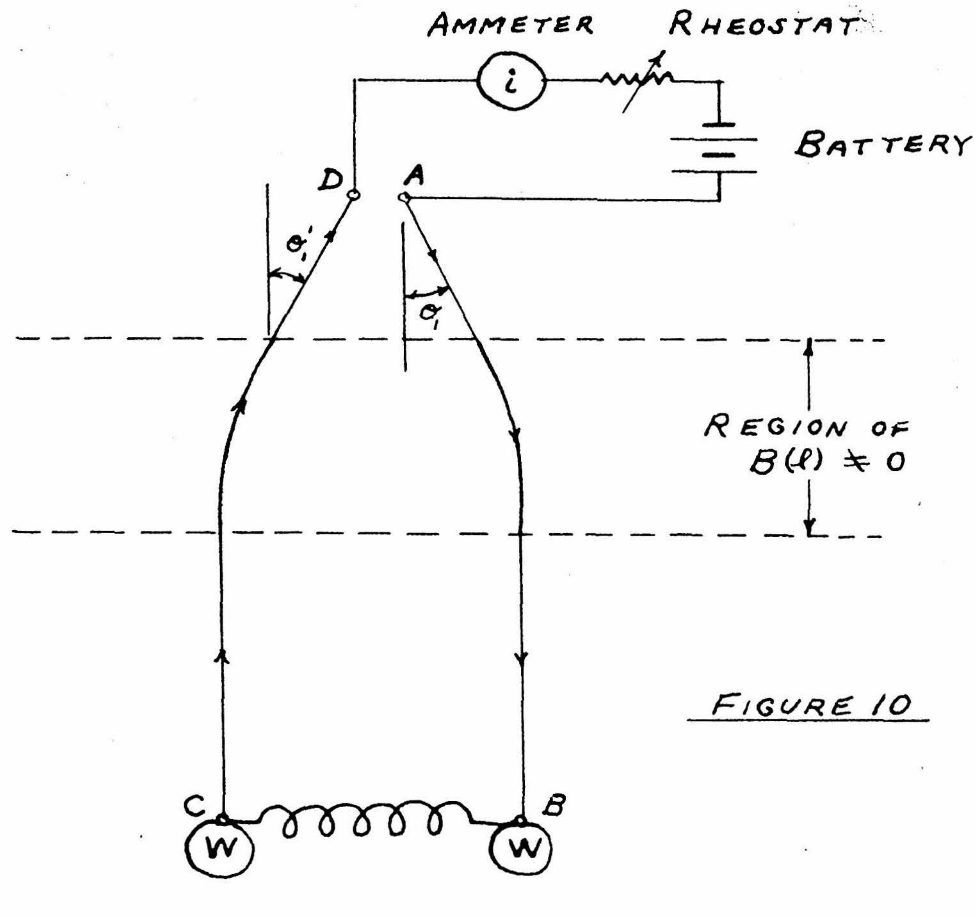

FIGURE 10

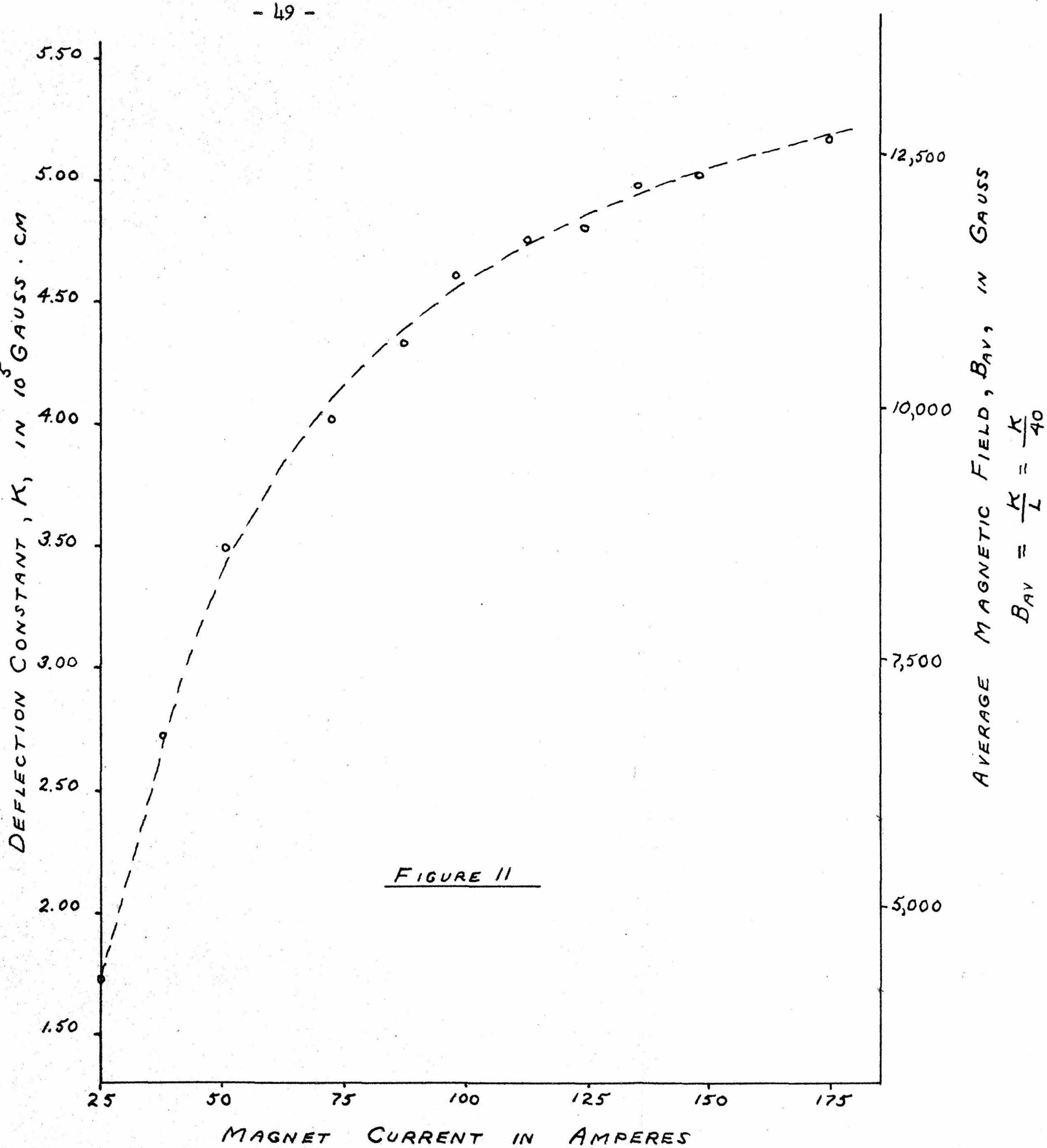
5.50
5.00
4.50
4.00
3.50
3.00
2.50
2.00
1.50
DEFLECTION CONSTANT, K, IN 10^5 GAUSS · CM
12,500
10,000
7,500
5,000
AVERAGE MAGNETIC FIELD, B_{AV}, IN GAUSS
$B_{AV} = \frac{K}{L} = \frac{K}{40}$
25
50
75
100
125
150
175
MAGNET CURRENT IN AMPERES

FIGURE 11

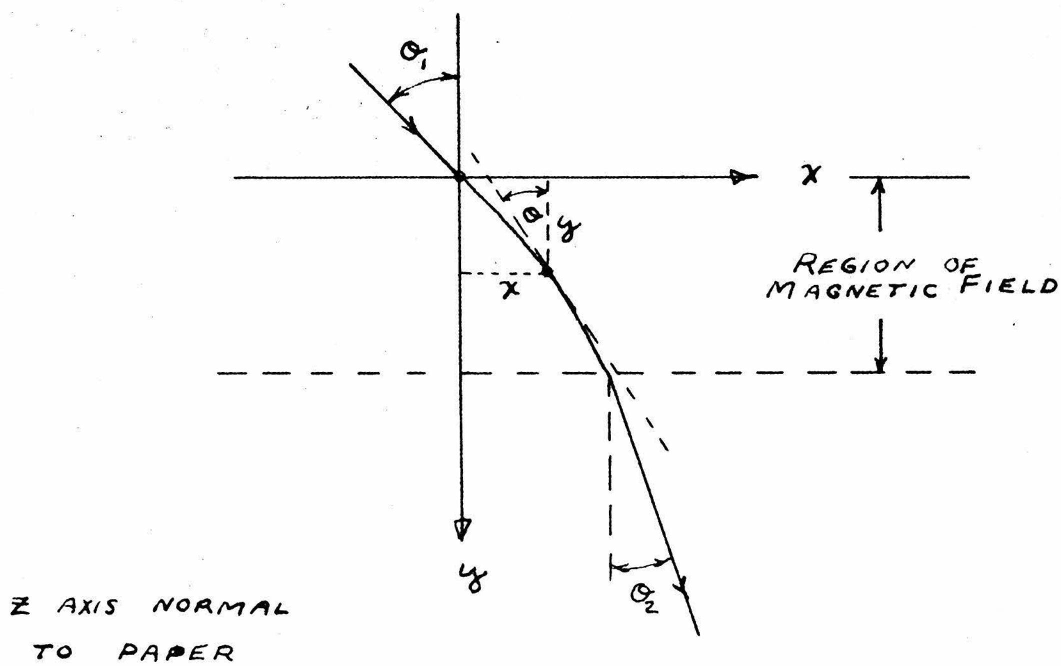

θ_1
x
θ
y
x
REGION OF MAGNETIC FIELD
y
θ_2
Z AXIS NORMAL TO PAPER

FIGURE 12

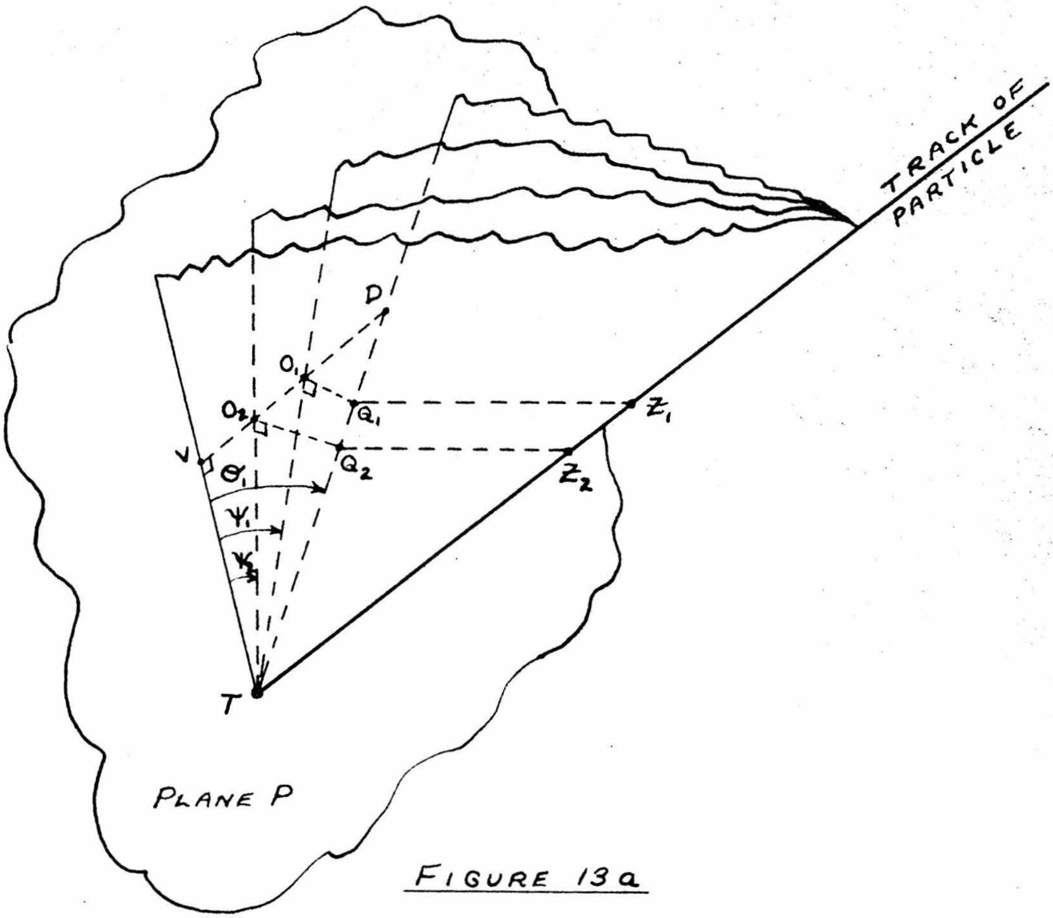

FIGURE 13a

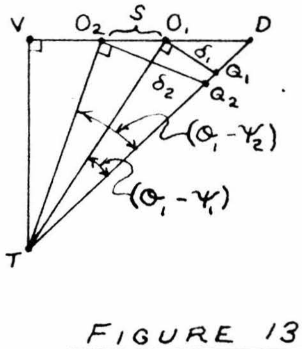

PLANE P IN PLANE OF PAPER

FIGURE 13b

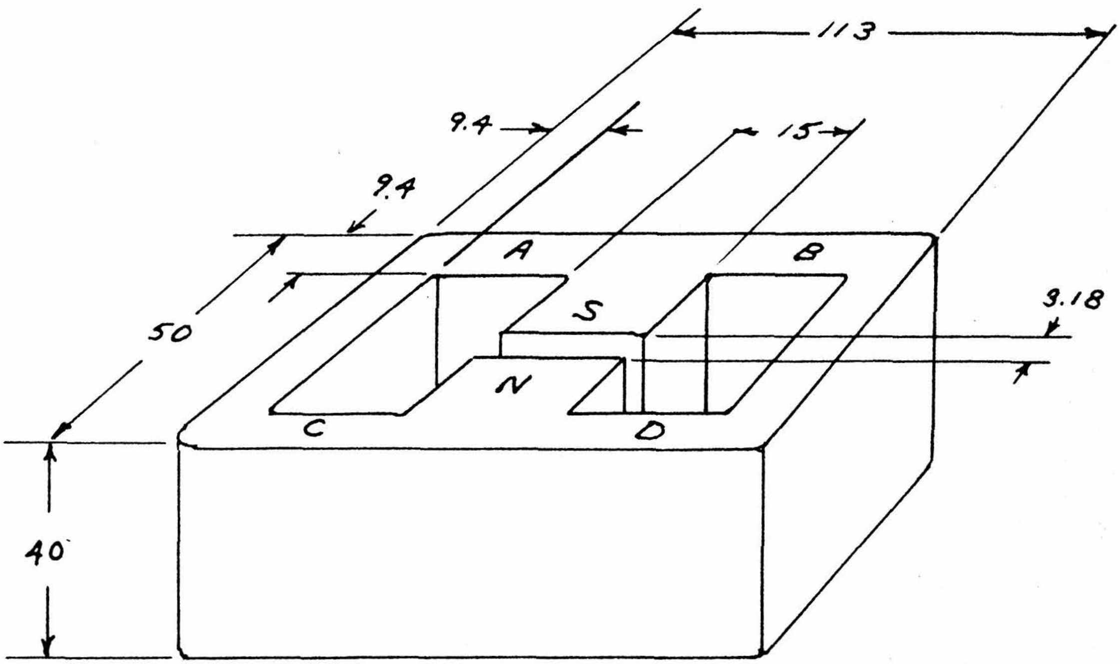

MAGNET DIMENSIONS
(IN CM)

FIGURE 14